



# Effect of higher deposition temperatures on the microstructure and mechanical properties of Al 2024 cold sprayed coatings

Paloma Sirvent<sup>a,\*</sup>, Miguel A. Garrido<sup>a</sup>, Claudio J. Múñez<sup>a</sup>, Pedro Poza<sup>a</sup>, Simone Vezzù<sup>b,1</sup>

<sup>a</sup> DIMME – Durability and Mechanical Integrity of Structural Materials, Escuela Superior de Ciencias Experimentales y Tecnología, Universidad Rey Juan Carlos, c/Tulipán s/n, Móstoles, 28933 Madrid, Spain

<sup>b</sup> Veneto Nanotech scpa, Nanofab Laboratory, via delle Industrie, 5, 30157 Marghera, Italy

## ARTICLE INFO

### Keywords:

Aluminum alloy  
Cold spray  
Electron microscopy  
Micro/-nanoindentation

## ABSTRACT

Cold spray is a coating technology that works at temperatures below the melting point of the initial powder and appears to be an interesting alternative to repair aeronautical components. This work evaluates the effect of temperature on the quality and properties of the aluminum alloy 2024 coatings deposited by cold spray. The coatings were sprayed at a conventional temperature of 350 °C and at a non-conventional one of 500 °C on aluminum 2024 T351 substrates. Electron microscopy was used to analyze the microstructure. Depth sensing indentation and Vickers microhardness tests were conducted to determine the elastic modulus and hardness. Both coatings exhibited a work hardened microstructure, and no modifications in phase composition were observed. However, the coating processed at 500 °C presented hardness values lower than those obtained for the coating processed under conventional conditions. The hardness of the coatings increased regarding to the initial powder particles due to the plastic deformation induced during spraying. Comparing both coatings, the study indicates that cold spray at 500 °C could be adequate for maintaining and overhauling aluminum components used in the aeronautical industry.

## 1. Introduction

Aluminum alloy 2024 (Al 2024) is extensively used in aeronautical components in which high strength and light weight are necessary [1,2]. Traditionally, these components are replaced when their reliability is compromised due to wear or damage, which increases maintenance costs. Therefore, the development of reliable repair techniques for the aeronautical industry is especially important. Nowadays, coating deposition methods are being studied as a less expensive and more environmentally friendly alternative of maintenance so the local damage is repaired without replacing the entire component [3,4].

Welding and thermal spray techniques have already been used for maintenance operations but have certain associated limitations. Most of these methods work at high temperatures (over the melting point of the initial feedstock powder). These deposition temperatures can favor the development of tensile residual stresses and oxidation during the coating generation, thereby promoting a reduction in their fatigue performance by cracks propagation and the appearance of undesirable phases [5]. However, cold gas dynamic spray (CGDS), or simply cold spray (CS), is a coating technology that works at temperatures below

the melting point of the initial powder and appears to be an interesting option to repair these aeronautical components while avoiding the detrimental effects of high temperature [6–8].

The bonding effect facilitated by the high temperatures reached in high temperature thermal spray techniques, such as Plasma Spray or High Velocity Oxi-Fuel, is replaced in CS by the increase in the particle deposition velocity. The particles are accelerated using a preheated compressed gas (air, nitrogen, helium or a mixture therein). This particle and gas flow is conducted through a de Laval nozzle to enhance the velocity. The high impact velocities of the particles (between 200 and 1200 m/s) on the substrate enable the coating development because of the plastic deformation of the particles [6]. Thus, powder particles become embedded and generate coatings by the stacking of the sprayed material. The lower temperatures provide coatings with a reduced oxidation, lower tensile residual stresses and avoid the formation of undesirable phases, maintaining the initial composition of the powder [6,8]. Therefore, the development of thick coatings is permitted, which is promising for repairing purposes.

The process gas type, temperature, pressure and stand of distance (SOD) along with the nozzle are the primary manufacturing parameters

\* Corresponding author.

E-mail addresses: [paloma.sirvent@urjc.es](mailto:paloma.sirvent@urjc.es) (P. Sirvent), [miguelangel.garrido@urjc.es](mailto:miguelangel.garrido@urjc.es) (M.A. Garrido), [claudio.munez@urjc.es](mailto:claudio.munez@urjc.es) (C.J. Múñez), [pedro.poza@urjc.es](mailto:pedro.poza@urjc.es) (P. Poza), [vezzu@live.it](mailto:vezzu@live.it) (S. Vezzù).

<sup>1</sup> Current address: Air Liquide Welding Italy, Loc. Casalmenini 3 37010 Rivoli Veronese, Italy.

**Table 1**  
Size and chemical composition data of the Al 2024 powder provided by the manufacturer.

Al 2024 powder									
Size ( $\mu\text{m}$ )	20–63								
Element composition	Al	Cu	Mg	Si	Fe	Mn	Cr	Zn	Ti
wt. (%)	Balance	3.8–4.9	1.2–1.8	0.5	0.5	0.3–0.9	0.1	0.25	0.15

that control the quality of the CS coatings. The appropriate values of these parameters are unique for each sprayed material. Thus, coating optimization for a more efficient deposition and better coating performance is primarily focused on the choice of the adequate deposition parameters. Other factors, such as the morphology or size of the sprayed particles or surface pretreatments of the substrate, also influence the coating performance [6,8,9].

In recent years, coatings of aluminum (Al) alloys sprayed by CS have been investigated using different deposition parameters to develop well-bonded coatings with low porosity [10–18]. A range of process gas temperatures between 200 °C and 450 °C have been previously used to deposit this material. Ziemain et al. [12] studied the effect of substrate surface roughening and CS coating on the fatigue life of AA2024 specimens. The coating was generated by powder particles accelerated with a nitrogen carrier gas at a temperature of 230 °C and 3.45 MPa pressure. Rokni et al. [19] deposited nanocrystalline 5083 Al powder via helium as the process gas. In this study, the pressure and temperature of helium were maintained at 20 bar and 450 °C at the heater exit, respectively. This high temperature was used in order to decrease the critical impact velocity needed to deposit this nanocrystalline powder. Nevertheless, to the best of the authors' knowledge, there are no studies examining the use of higher deposition temperatures for Al alloys. The application of higher deposition temperatures is interesting because the thermal softening of the particles has been reported to facilitate the bonding process to increase the deposition efficiency [8,20–22]. The bonding of the coatings in CS is based on the deformation of the particles that could be enhanced by the thermal softening.

T. Stoltenhoff et al. [20] developed models of the gas and particle flow fields for the CS process. This study determines the increase in the particle velocity ( $v_p$ ), temperature ( $T_p$ ), and deposition efficiency (DE) with the increase in the deposition temperature using fluid dynamic calculations. For example, increments of 30 m/s for  $v_p$  and 50 °C for  $T_p$ , lead to a 25% increment on DE for copper CS coatings sprayed under certain conditions. T. Schmidt et al. reported experimental work [21], based on the previous quoted models [20], that also demonstrates the improvements in strength and electrical conductivity for copper CS coatings when spraying at higher temperatures. In addition, G. Bae et al. [22] confirmed the enhancement of the adhesive and cohesive bonding on Ni CS coatings when the Ni particles are thermally softened, verifying their previous results of a finite element model.

Therefore, the aim of this work is to study the effects of increasing the spraying temperature on the quality of Al 2024 coatings deposited by CS on substrates of the same alloy. For this purpose, the microstructure and mechanical performance have been investigated on Al 2024 coatings sprayed at a conventional temperature of 350 °C and at a non-conventional temperature of 500 °C. The microstructure was analyzed using scanning and transmission electron microscopy to evaluate the differences in the deposition created by increasing the gas process temperature. Conversely, the mechanical performance was evaluated by depth sensing indentation and Vickers microhardness tests to study the evolution of the elastic modulus (E) and hardness (H) with the gas process temperature. Both the microstructure and mechanical properties obtained from the coatings have been compared to those obtained from a substrate of Al 2024 T351, the material used in aeronautical components. The primary goal of this work is to evaluate the effects of temperature on the viability of CS for the maintenance and overhaul of

aeronautical components by comparing the CS coating performance to that observed in the substrate.

## 2. Materials processing

### 2.1. Raw materials

Al 2024 coatings were deposited onto Al 2024 substrates with the aim of studying the application of coatings deposited by CS for repairing Al components. Commercially available gas-atomized Al 2024 powder (TLS Technik GmbH, KG, D-06733 Bitterfeld, Germany) was used for the deposition. The composition of the particles reported by the supplier is shown in Table 1. The particles were characterized by spherical geometry (Fig. 1a) with a size distribution mainly ranged between 20 and 63  $\mu\text{m}$  (Table 1). The substrates were supplied by AVIO AERO (GE Aviation) with aeronautical grade and in T351 temper. The surface coated by CS was 50 mm  $\times$  50 mm and the thickness was 4 mm. The standard surface preparation, consisting of a grit blasting process, was carried on the substrates [23]. The average roughness of their surfaces,  $R_a$ , was  $17.17 \pm 1.88 \mu\text{m}$  measured by a profilometer (SurfTest SJ-301, Mitutoyo, Japan).

### 2.2. CS deposition

The depositions were performed with a CS system Kinetiks 4000 (CGT Cold Gas Technology, Ampfing, Germany) using nitrogen as the process gas. A Polybenzimidazole (PBI) polymeric nozzle designed for Al powder spraying was used at 350 °C at a pressure of 3.75 MPa, as mainly used up today for the Al alloy deposition [15]. The process gas temperature is limited by the polymeric nature of the nozzle material. To surpass this limitation, a silicon carbide nozzle, developed by Impact Innovations GmbH (Haun/Rattenkirchen, Germany) equipped with a customized water cooling system (Impact Innovations) was installed on the CS Kinetiks 4000 and used at the higher process gas temperature. This second configuration of CS with the SiC nozzle and water cooling was tested up to 650 °C while preserving the same feedstock material, confirming the suitability of the equipment configuration, even if the process stability progressively decreases as a function of process gas temperature due to the progressive clogging of the nozzle. The two major contributions causing nozzle clogging are the characteristics of the feedstock material in terms of such parameters as composition, melting temperature, and particle size and shape, as well as the process gas temperature. The higher process gas temperature increases the particle adhesion to the walls of the nozzle, particularly near the throat both at the converging and diverging parts where the intensity of particle-wall collisions is relevant. Thus, the operating temperature was selected as 500 °C to balance the desired enhanced particle softening and the process stability to ensure a reliable and repeatable deposition process. At this temperature, the capability to have a stable process for up to 1 h of consecutive spraying is reported, which is sufficient to complete a typical repair of aeronautical applications. A second parameter that was tuned for optimization was the nozzle traverse speed, which has been experimentally tuned in order to preserve substrate temperature lower than 150 °C. At the lower temperature, 50 mm/s traverse speed was used. At the higher temperature, a traverse speed of 100 mm/s was set to mitigate the thermal input to the substrate induced by the hot process gas flow, which is detrimental to the base material

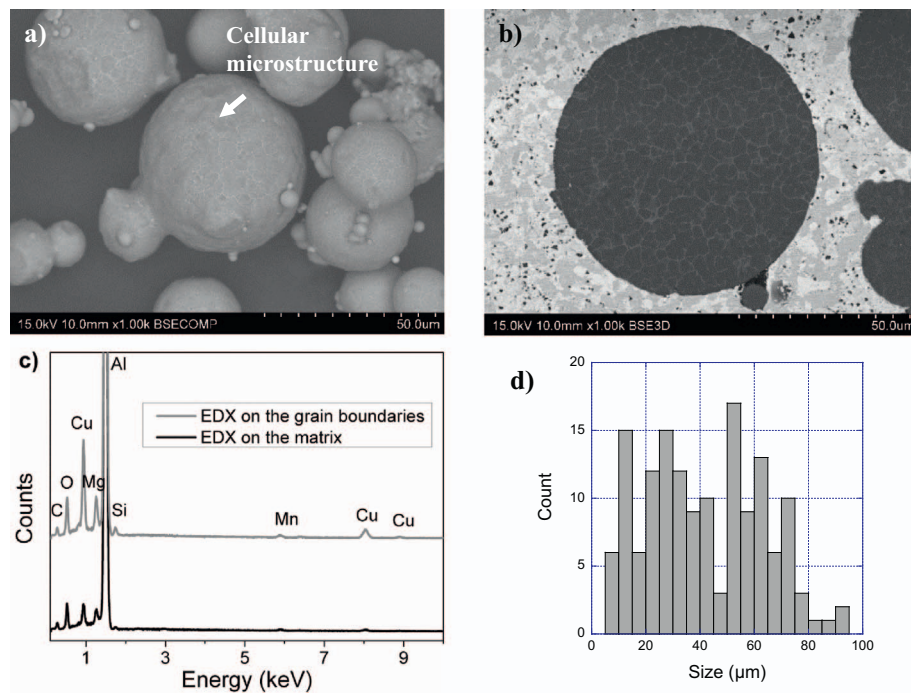


Fig. 1. SEM images of a) the external morphology and b) the cross-sectional view of the as-received Al 2024 powder embedded in a Sn matrix where a cellular grain structure is revealed. c) The EDX spectra collected on the grain boundaries and on the matrix of the cross-section of a particle. d) Size distribution of the Al 2024 powders used in the deposition process.

Table 2  
CS deposition parameters.

Nozzle material	PBI (air cooled)	SiC (water cooled)
Gas temperature (°C)	350	500
Gas pressure (MPa)	3.75	3.75
Gas quantity (m <sup>3</sup> /h)	115	110
Feeder (r.p.m.)	3.5	3.5
Feeder gas flow (m <sup>3</sup> /h)	5	5
Powder feed rate (g/min)	18	18
SOD (mm)	20	20
Spray angle (°)	90	90
Traverse speed (mm/s)	50	100
Total spray time (s)	1210	605
Total amount of powder (g)	400	200
Preheat	None	None

characteristics and microstructure, as well to the development of the heat affected zones and residual stresses. The set of spray parameters are summarized in Table 2.

### 3. Experimental

#### 3.1. Microstructural characterization

A metallographic preparation of the coatings was conducted on their transversal cross-section (parallel to the spraying direction) for the microstructural investigation. Samples were cut with an alumina cut-off wheel and mounted in a low-stiffness resin. Next, the samples were smoothed and polished in a multistep process to a mirror finish using a last suspension of 0.05 μm of alumina [24]. The substrate material was prepared using a metallographic procedure that was similar to the previous one used for the coatings. The substrate was chemically etched by immersion in Keller's reagent (95 mL water, 2.5 mL HNO<sub>3</sub>, 1.5 HCl, 1.0 HF) for 10–20 s.

The cross-sections of the powder particles were prepared using a relatively stiff matrix based on a Sn alloy as the mounting material. The use of Sn to embed the powder is justified in the 3.2 epigraph of this section about the mechanical characterization of the particles. The mounting process with Sn was carried out in two steps. The alloy was

initially melted by heating it to 250 °C, the lowest temperature necessary to melt the Sn alloy to minimize its possible effect on the microstructure of the Al particles. The particles were added and the mixture was air cooled to room temperature. The embedded powder was metallographically prepared by polishing following a procedure similar to the one described for the coatings and the substrate.

An optical microscope (OM, Motic, Xiamen, China) and image analysis software were used to measure the thickness and porosity of the coatings. Three images were taken on three different areas along each coating to measure their thicknesses. The average thickness and standard deviation were obtained using 30 measurements (10 per image). The average values and standard deviations of the porosity were obtained from three images acquired at 50× from each coating.

Scanning electron microscopy (SEM, S-3400, Hitachi, Tokyo, Japan) and energy dispersive X-ray microanalysis (EDX, Bruker detector) were used to study the microstructure and chemical composition of the particles, substrate and coatings. Secondary electron (SE) and back-scattered electron images (BSE) were taken. The size of the particles was evaluated measuring the diameter of 50 particles from two different SEM images, which provided the distribution of the particle diameters. The grain size of the powder was measured using image analysis on the cross-sections of the particles following the requirements of the ASTM E1382 standard [25]. The grain size was calculated using the Intercept and Intersection Count Method, which consists of counting the number of grain boundary intersections by a circular test. This reticle consists of three concentric circles with a total line length of 500 mm. The ASTM grain size number, G, was originally defined as:

$$N_{AE} = 2^{G-1} \quad (1)$$

where  $N_{AE}$  is the number of grains per square inch at 100× magnification [26].

Transmission electron microscopy (TEM, Tecnai 20, Philips, Eindhoven, The Netherlands) linked with an EDX detector was used to analyze the fine microstructure on the coatings and substrate. Longitudinal sections were prepared for the analyses that were parallel to the deposition plane in the case of the coatings. Discs with a 3-mm diameter were thinned to 100 μm in thickness by mechanical polishing. The final thinning was conducted by electropolishing using an electrochemical polisher (Tenupol-5, Struers, Ballerup, Denmark). A

solution of nitric acid (30 vol%) in methanol (70 vol%) was used as the electrolyte by applying 20 V at  $-10^{\circ}\text{C}$ . The TEM study involved the use of bright field (BF), dark field (DF) and high-resolution transmission electron microscopy (HRTEM) images, and the analysis of the electron diffraction patterns (EDP) obtained by selected area (SADP) and nanobeam electron diffraction (NBDP).

The structural characterization of the powders, substrate and as-sprayed coatings was conducted by X-ray diffraction (XRD, PW3040/00 X'Pert MPD/MRD, Philips, Eindhoven, The Netherlands). The diffraction patterns were recorded using an angle step of  $0.02^{\circ}$ . The angle width varied from  $15^{\circ}$  to  $115^{\circ}$  for the substrate and coatings experiments and from  $15^{\circ}$  to  $90^{\circ}$  for the powder.

### 3.2. Mechanical characterization

Depth sensing indentation tests were conducted on the powder particles, substrate and coatings to measure the H and E. The tests were performed by a Nanoindenter Agilent G200 (Keysight, Arizona, USA) using a new Berkovich diamond indenter with a nominal tip radius of 20 nm. During this test, the material to be characterized is indented by a tip of known geometry during a loading and unloading cycle. For this cycle, the load and the penetration depth of the indenter are continuously recorded obtaining force-displacement data [27]. In this work, the continuous stiffness measurement (CSM) indentation methodology was used. This technique superimposes continuous loading and unloading cycles during the main loading branch with a frequency of 45 Hz and a 2 nm of displacement. The Oliver-Phar methodology [27] was applied to each unloading phase to obtain the evolutions of E and H versus the penetration depth (h). A commercial Al 2024 alloy ( $E = 70\text{ GPa}$ ) was used for the calibration procedure to obtain the actual contact area ( $A_c$ ) as a function of the contact depth ( $h_c$ ) [28]. Two different calibrations were performed: one was conducted up to 600 nm for the particle indentations, and the other was up to 2000 nm for the coating and substrate tests.

The indentation tests on the powder were conducted on the particle cross sections after they were embedded in a Sn alloy and metallographically prepared. The choice of Sn is based on an excellent combination of low melting temperature and relatively high stiffness. The use of a relatively stiff matrix compared to the Al 2024 alloy makes it possible to discriminate the indentation data that are consistent with the particle response over those that are influenced by the matrix. Thirty tests were performed, each on a different particle. The larger diameter particles were selected for the tests to avoid edge effects. Although the maximum h was set at 600 nm, only data showing a linear correlation between the harmonic contact stiffness (S) and h were selected for the analysis [29]. The indentation size effects (ISE) [30,31] on the H measurements was corrected using the proportional specimen resistance (PSR) model [32]. This model estimates the load independent of H, known as true hardness ( $H_0$ ), by means of a parameter,  $a_2$ , which is determined as the slope of the ratio load (L) versus the  $h_c$  (Eq. (2)). The relation between the  $H_0$  and the parameter  $a_2$  is determined by Eq. (3), where  $h_c$  and  $A_c$  are the contact depth and the contact area at the point of the maximum indentation, L.

$$L/h_c = a_1 + a_2 h_c \quad (2)$$

$$H_0 = a_2 (h_c^2/A_c) \quad (3)$$

The E and H values of the coatings and the substrate were measured on the longitudinal cross-sectional view (parallel to the deposition plane of the coatings). The samples were prepared following a similar procedure to that employed for the microstructural characterization. Sixty indentation tests were carried on the substrate in a square matrix of  $6 \times 10$  measurements spaced at  $80\text{ }\mu\text{m}$ . For the coatings, two matrices of  $8 \times 5$  indents (a total of 80 tests) were conducted, with each indent being spaced at  $100\text{ }\mu\text{m}$ . The maximum h was set at 2000 nm for all the tests. The data range used for calculations was selected by applying the

same criterion used for the indentation measurements on the powder particles.

The Vickers microhardness (HV) was measured using a Buehler 2101 microdurometer on the transversal cross-section of the coatings (perpendicular to the deposition plane) to evaluate the possible variations in H in terms of the distance from the interface. Samples were polished following the same metallographic preparation as the method used for the microstructural analysis. Three HV profiles were obtained after performing tests from the interface with the substrate until measuring the surface every  $50\text{ }\mu\text{m}$ , being spaced to avoid interactions between measurements. The HV value given for each distance from the interface is the average of the three measurements performed at that distance. The indentation tests were conducted by applying a load of 50 gf and following the recommendations of the ISO 6507-1:2006 standard. The indentation profiles were also extended along the substrate to obtain an H reference value.

## 4. Results

### 4.1. Microstructure characterization

#### 4.1.1. Powder microstructure

Fig. 1a shows the morphology of the Al 2024 initial feedstock powder, which was characterized mostly by spherical particles with some irregular ones included, as well. The particle diameter showed a distribution in which 68% of the particles had a diameter between 20 and  $62\text{ }\mu\text{m}$ . The minimum and maximum values of the diameters were 5 and  $91\text{ }\mu\text{m}$ , respectively. The SEM images of the particles revealed that a cellular grain structure was observed on the external surface (Fig. 1a). A similar structure was observed on the cross-section of the particles (Fig. 1b). A higher content of Cu and Mg was observed at the grain boundaries by the EDX analysis (Fig. 1c). The size distribution of the Al 2024 powders used for the CS spraying process is shown in Fig. 1d. This distribution is in agreement with the powder size range provided by the manufacturer (Table 1). The XRD analysis on the powder only identified the face centered cubic (FCC) Al structure (Fm-3m space group,  $a = 4.049\text{ }\text{\AA}$ ) (Fig. 2). The particles showed a grain size characterized by a G value of  $13.25 (\pm 0.28)$  according to the ASTM E1382 standard. This G value corresponds with a grain size between 3.0 and  $3.5\text{ }\mu\text{m}$  [26].

#### 4.1.2. Substrate microstructure

The XRD pattern analysis on the substrate only showed peaks

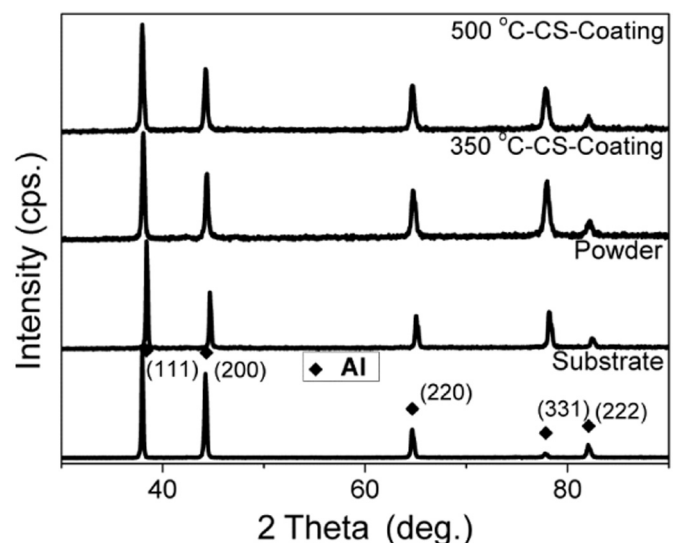


Fig. 2. XRD diffraction patterns of the Al 2024 T351 substrate, Al 2024 powder and CS Al 2024 coatings processed at 350 and  $500^{\circ}\text{C}$ .



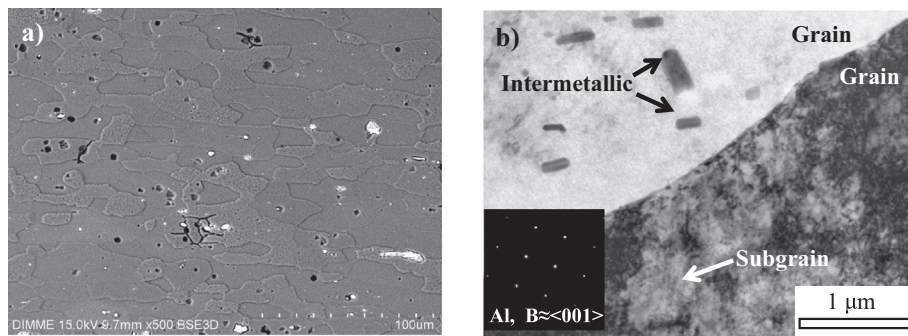


Fig. 3. a) SEM image of the etched microstructure of the Al 2024 T351 substrate. b) BF image of the Al 2024 T351 substrate showing the grain boundary between two Al grains. The observed intermetallics are indicated in the upper grain. The SADP of the darkest grain is also included which is oriented along  $B \approx \langle 001 \rangle$  direction.

corresponding to the Al FCC structure (Fig. 2). The microstructure of the substrate was formed by elongated grains that were larger than 100  $\mu\text{m}$  (Fig. 3a).

The TEM investigation confirmed the presence of large grains in the substrate which were formed by smaller subgrains, as it could be observed in Fig. 3b where the dark Al 2024 grain is oriented along  $B \approx \langle 001 \rangle$ . An intermetallic phase was also observed inside the Al 2024 grains (Fig. 3b). This phase was identified as  $\text{Al}_{20}\text{Cu}_2\text{Mn}_3$  (orthorhombic,  $a = 2.4 \text{ nm}$ ,  $b = 1.2 \text{ nm}$ ,  $c = 0.77 \text{ nm}$ ), being a phase typically observed in Al 2024 alloys [1,33,34].

#### 4.1.3. Coatings microstructure

The structure of the CS Al 2024 coatings was analyzed by XRD (Fig. 2), and only the peaks corresponding to the Al FCC structure were identified. No structural variations could be detected, even after spraying at 500  $^{\circ}\text{C}$ , with respect to the feedstock powders and substrate material. Thickness measurements showed that the coating processed at the highest temperature, 500  $^{\circ}\text{C}$ , was thinner ( $751 \pm 26 \mu\text{m}$ ) than the one processed at 350  $^{\circ}\text{C}$  ( $823 \pm 16 \mu\text{m}$ ).

The coatings exhibited a high quality with very low porosity levels and no delamination at the interfaces with the substrate (Fig. 4a and b) or between splats (Fig. 4c and d). Fig. 4c and d show that the microstructure of the CS Al 2024 coatings was composed of splats formed by small grains, ranging from the submicron to a few microns in size. This result is evidence of plastic deformation, which is expected after CS

[35]. Porosity values of  $0.75 \pm 0.09\%$  and  $0.41 \pm 0.07\%$  were measured on the coatings sprayed using 350  $^{\circ}\text{C}$  and 500  $^{\circ}\text{C}$  process gas temperatures respectively. The splats showed pancake morphologies (Fig. 4c and d) with more equiaxed grains in their interiors and elongated grains at their grain boundaries (GBs). As seen in Fig. 5a and b, the GBs in the CS coatings were enriched in Cu and Mg, indicating that the GB solute segregation in the feedstock powder was retained in the coatings [17,36].

The coatings processed at 500  $^{\circ}\text{C}$  presented a slightly less distorted microstructure with respect to the 350  $^{\circ}\text{C}$  CS coatings (Fig. 4c and d). The higher temperature reduces the particle yield strength, but it could also activate the dynamic recovery mechanisms, which promotes a less hardened microstructure.

The CS coating fine microstructure was analyzed by TEM. The obtained results showed a different microstructure compared with the Al 2024 T351 substrate due to the plastic deformation introduced during the deposition process. Fig. 6 shows TEM micrographs that illustrate the presence of subgrains in the microstructure of the CS. During the CS, the Al 2024 was plastically deformed, and consequently, dislocations interacted to form walls, networks and finally subgrain boundaries. However, as seen in Fig. 6, the size of these substructures increased (from 40 to 100 nm) as the gas temperature was increased (from 350 to 500  $^{\circ}\text{C}$ ). This result pointed to a less distorted microstructure in the coatings sprayed at the lowest temperature.

Fig. 7 shows the dislocation structures in the coatings processed at

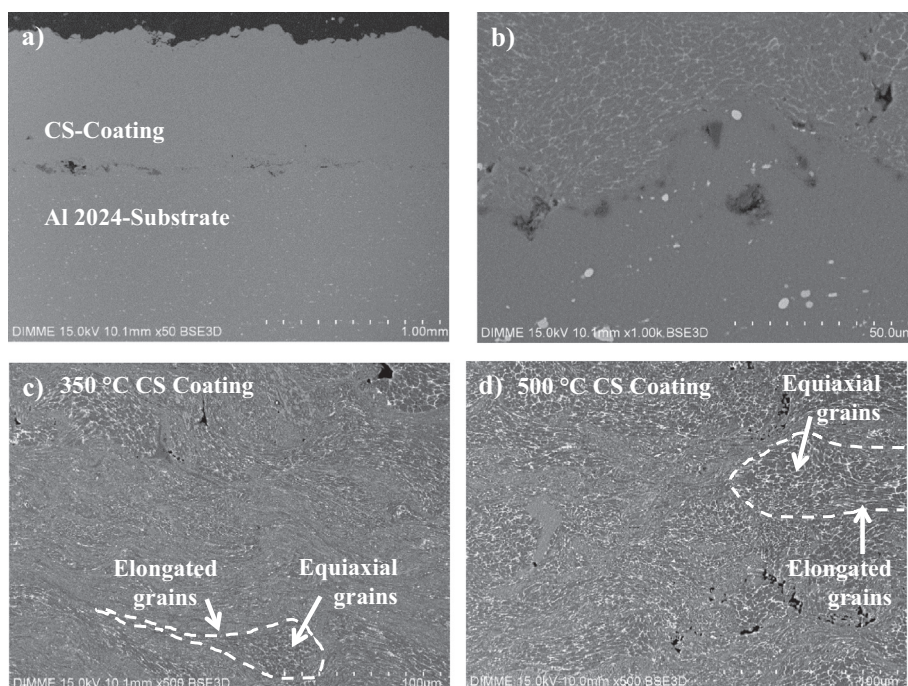


Fig. 4. SEM images of the a) cross-sectional view and b) interface of the CS-coating processed at 500  $^{\circ}\text{C}$ ; and SEM images of the splat microstructure of the c) 350  $^{\circ}\text{C}$  CS-coating and the d) 500  $^{\circ}\text{C}$  CS-coating. The morphology of a splat is highlighted in (c) and (d) figures by a dotted line and equiaxed and elongated grain regions are indicated by arrows.

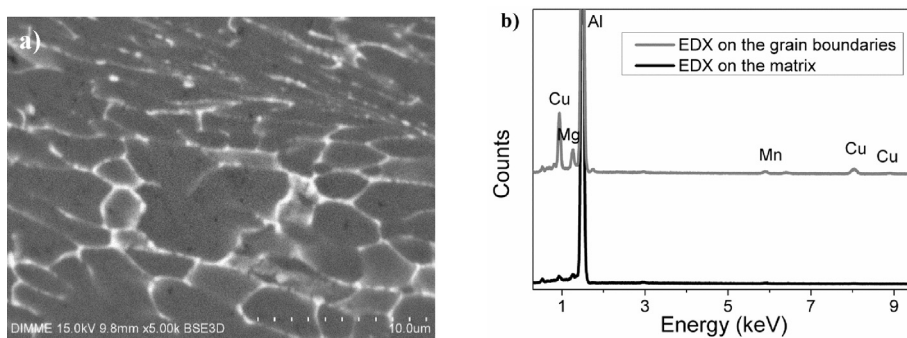


Fig. 5. SEM images of the 350 °C CS Al 2024 coating showing a) the grain structure inside the splats; and b) the EDX spectrum on the Al matrix and the grain interfaces.

350 °C (Fig. 7a) and 500 °C (Fig. 7b). The evolution of the dislocation structures during CS, forming walls, networks and finally subgrains, is almost completed in the coating processed at 350 °C. In this case, dislocations are mainly located at the subgrain boundaries. On the other hand, dislocation networks were clearly observed in the coatings processed at 500 °C.

The resulting microstructure appears to be less distorted in the coatings processed at a higher temperature, and the subgrain size is increased in these materials. Dislocation mobility is higher for the highest temperature and recovery mechanism should be activated reducing dislocation density. Consequently, the subgrain size is higher in the coatings processed at 500 °C.

$\text{Al}_2\text{Cu}$  (tetragonal, space group  $I4/mcm$ , 0.61 nm,  $c = 0.49$  nm) and  $\text{Al}_{20}\text{Cu}_2\text{Mn}_3$  precipitated at the grain and subgrain boundaries, as shown in Fig. 8. These precipitates were identified by EDP and EDX microanalysis and are typically observed in Al 2024 bulk alloys [1,33,34,37].

#### 4.2. Mechanical characterization

The indentation tests on the particles showed that the data available for the E and H calculations was sufficient to obtain reliable values for both properties. The plot of S vs. h showed a linear correlation between 200 and 400 nm (Fig. 9). From these data, an E of  $68.4 \pm 4.3$  GPa was calculated. The  $H_0$  was estimated by applying the PSR model because the selected data range was affected by the ISE, the H decreased with the penetration depth when increasing the load (Fig. 10a). The linear fitting of the plot of  $L/h_c$  against  $h_c$  for these indentation data showed a correlation of 0.99, verifying the suitability of the PSR model (Fig. 10b). The obtained nanohardness value of the particles was  $0.91 \pm 0.20$  GPa.

No resin effects were noticeable on the indentation tests conducted on the coatings (Fig. 11a). The data ranging between 300 and 2000 nm were used to calculate the mechanical properties. In addition, the plot of the H vs. h showed an asymptotic H value (Fig. 11b).

The depth sensing indentation results (Fig. 12 and Table 3) showed that the E of the coatings was in the range of the E of the particles, which was also similar to the one of the substrate material

( $67.6 \pm 1.8$  GPa). The coatings' H was enhanced with respect to the feedstock powder, and a more marked increase in H was obtained on the 350 °C CS coating ( $1.43 \pm 0.19$  GPa). The H of the 500 °C CS coating was  $1.14 \pm 0.11$  GPa and the H value of the substrate was  $1.25 \pm 0.06$  GPa, which was also harder than the powder particles. The H of the 350 °C CS coating exceeded that obtained on the substrate with a 12% increase.

The HV indentation profiles (Fig. 13 and Table 3) revealed that the H remained nearly constant along the full thickness of the coatings. The extension of the indentation profiles along the substrate showed that the HV linearly increased from a depth of 200  $\mu\text{m}$  until the interface with the coating. The average value of HV ( $H_{V_m}$ ) of the coating processed at 350 °C was slightly higher than that of the coating processed at the higher temperature.

#### 5. Discussion

The Al 2024 coatings were processed by CS at 350 °C and 500 °C. Both conditions promoted high quality coatings with low porosity and no delamination with the substrate nor between splats (Fig. 4). The microstructure of both coatings was typical of CS deposition. The impact of the particles with the substrate generates flat splats perpendicular to the impact [6]. The accommodation of the splats during deposition minimizes the porosity and eliminates possible delamination. The thickness of the coatings was affected by the temperature of the spraying process. Coatings processed at the highest temperature, 500 °C, showed smaller thickness values than those measured on coatings processed at 350 °C. These results were previously studied by Schmidt et al. [38]. According to the models proposed by Schmidt, increasing the gas temperature leads to a significant increase in particle velocity. This increment in particle velocity is responsible of an increase in particles which rebound on the surface with consequent higher contribution of erosion.

The particle size was ranged from 20  $\mu\text{m}$  to 63  $\mu\text{m}$  (Table 1). The critical velocity for Al particles of 20  $\mu\text{m}$  ranged from 620 m/s to 660 m/s, according to Sova et al. [39]. They reported Al particle velocities along the nozzle axis that were obtained for two different values of gas pressures, 2 and 3 MPa, for 20–40  $\mu\text{m}$  sized particles. For a gas

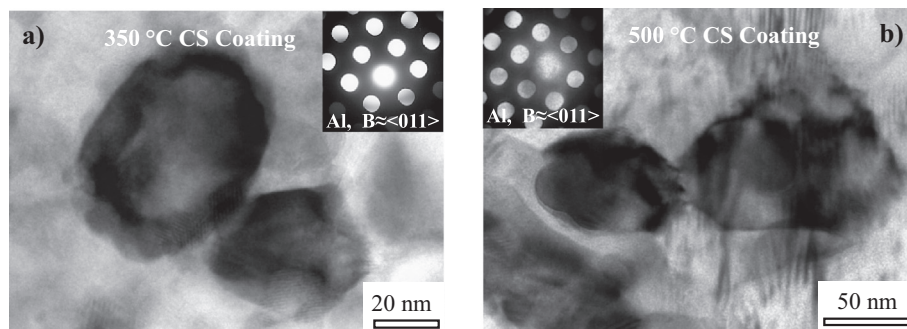


Fig. 6. BF images of CS Al 2024 coatings. a) Subgrains formed in the standard coating, including the NBEDP. b) Subgrains formed in the coating processed at 500 °C, including the NBEDP. The subgrain size is clearly reduced at lower temperature.



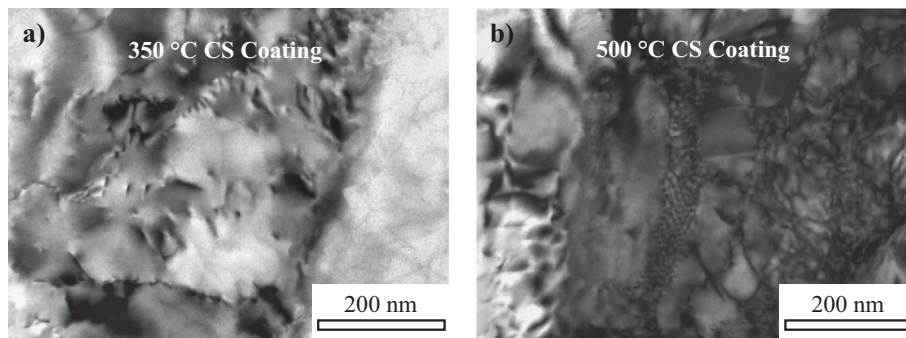


Fig. 7. a) BF image from the standard Al 2024 coating processed at 350 °C showing dislocation structures formed during the CS. b) A BF image showing dislocation networks after the CS at 500 °C.

pressure of 3 MPa, the particles velocity at the end of the nozzle ranged from 525 m/s for particles of 40  $\mu\text{m}$  to 700 m/s for particles of 20  $\mu\text{m}$ . Consequently, it is possible that the particles sprayed in the present study have reached the critical velocity. The higher the spraying temperature, the higher the spraying velocity, and consequently, the higher the number of particles whose velocity is higher than the critical one, favoring the erosion process during the spraying process at 500 °C.

However, the spraying temperature is not the only parameter that can influence the thickness of the coatings. The traverse speed could also have a relevant effect [40]. The relevance of this parameter on the coating thickness is related to the deposition efficiency of the spraying process. The deposition efficiency of powder increases as the traverse speed of the spraying nozzle decreases. However, the deposition efficiency increases linearly as the gas temperature increases [41]. Consequently, in this work, the higher speed used with the SiC nozzle was due to the relevant increment of the deposition efficiency achieved with the highest spraying temperature (Table 2).

The increased gas spraying temperature did not affect the phase composition of the coatings. The phase composition of the initial feedstock powder was shown to be maintained, even at the highest temperature that was used (500 °C). The primary phase structure identified by XRD was FCC Al on the powder particles and on both coatings (Fig. 2). Moreover, the grain structure observed on the interior regions of the splats (Fig. 5a) was shown to be similar to that of the initial feedstock particles (Fig. 1b). The observed cellular grain

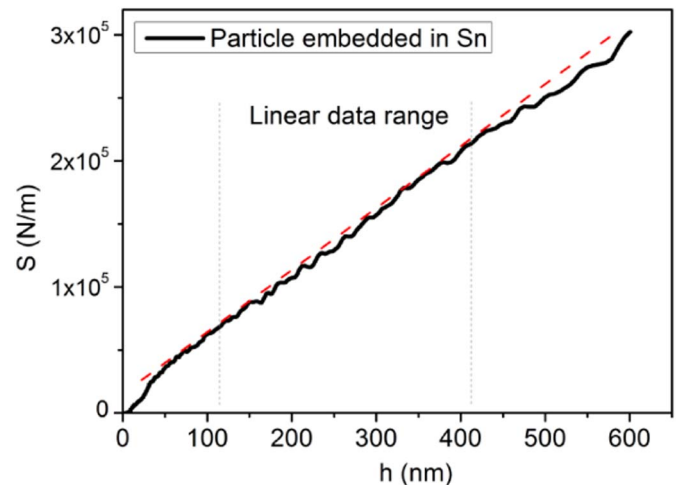


Fig. 9. Stiffness ( $S$ ) vs. penetration depth ( $h$ ) plot of an indentation test conducted on an Al 2024 particle embedded in a Sn alloy matrix.

structure is characteristic of the microstructure generated due a rapid solidification process [1], as the gas atomization followed for the powder fabrication [36,42]. Cu rich precipitates, identified as  $\text{Al}_2\text{Cu}$  and  $\text{Al}_{20}\text{Cu}_2\text{Mn}_3$  in the coatings, decorated the powders and coatings

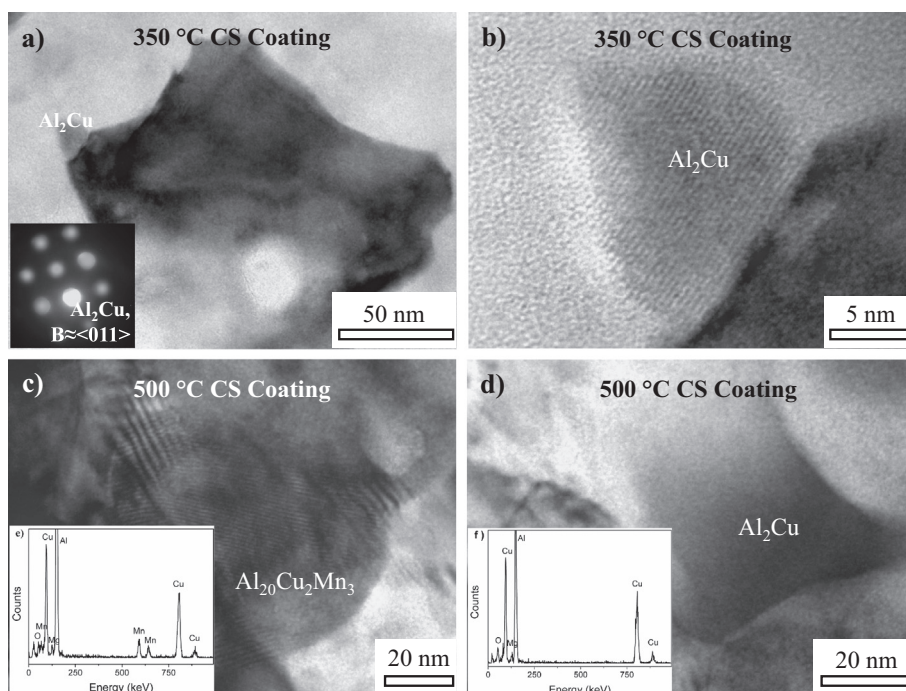


Fig. 8. a) A BF image showing the  $\text{Al}_2\text{Cu}$  precipitation at the subgrain boundaries in the standard CS Al 2024 coatings processed at 350 °C, including the NBEDP. b) A HRTEM image detailing the  $\text{Al}_2\text{Cu}$  precipitate presented in (a). c) A BF image showing the  $\text{Al}_{20}\text{Cu}_2\text{Mn}_3$  precipitation at the subgrain boundaries in the coating processed at 500 °C. d) A BF image showing the  $\text{Al}_2\text{Cu}$  precipitation at the subgrain boundaries in the coating processed at 500 °C. e) and f) EDX microanalysis of the  $\text{Al}_{20}\text{Cu}_2\text{Mn}_3$  and  $\text{Al}_2\text{Cu}$  precipitates, respectively.

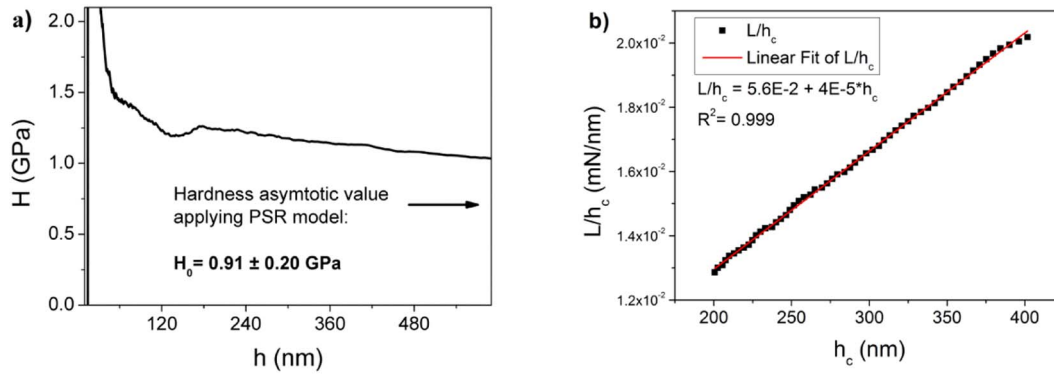


Fig. 10. a) The hardness (H) vs. penetration depth (h) plot of an indentation test conducted on an Al 2024 particle embedded in a Sn alloy matrix. b) Linear fit of the ratio of the load by the contact depth ( $L/h_c$ ) vs. the contact depth ( $h_c$ ) plot of the same indentation test, verifying the applicability of the PSR model.

grain boundaries (Fig. 1, Fig. 5 and Fig. 8). These phases are usually found in bulk Al 2024 alloys [1,37].

The main effect of the processing gas temperature from the microstructural point of view was detected at the dislocation structures observed by the TEM. The grains observed inside the splats were elongated and nearly disappeared at the splat interfaces due to the deformation process (Fig. 4c and d). This observation indicated that the deformation was more severe at the interfaces between splats. During the CS, reticular dislocation structures and dislocation walls were formed due to the plastic deformation of the spraying powders (Fig. 7). Finally, the dislocations structures promoted a cold worked microstructure formed by the subgrains. Thus, the subgrain boundaries appeared to have been generated through a polygonization process [43]. The absence of dislocations inside the smaller subgrains observed by TEM (Fig. 6) confirmed that these fine subgrains were formed from the transformation of the dislocation walls. The subgrain size increased as the temperature reached 500 °C, suggesting a less hardened microstructure (Fig. 6). Increasing the gas processing temperature dislocation mobility also increased and the dynamic restoration processes could be activated, leading to a more stable dislocation structure [11,17,44].

In agreement with the microstructural observations, the spraying temperature also affected the coating mechanical properties. Table 3 summarizes the E and H values (nanohardness and microhardness) of the substrate, powder and coatings processed at 350 °C and 500 °C.

The E measured in both coatings was similar to that obtained for the powder particles. However, the H increased as the powders were cold sprayed to form the coatings. In addition, the H values were higher in the coating deposited at 350 °C. The work hardened microstructure observed in the coatings explained the higher H values in the sprayed materials. The coating processed at 500 °C exhibited a less work hardened microstructure, explaining the smaller increment in the H from the values observed in the powder particles.

However, comparing the coatings H values with the values

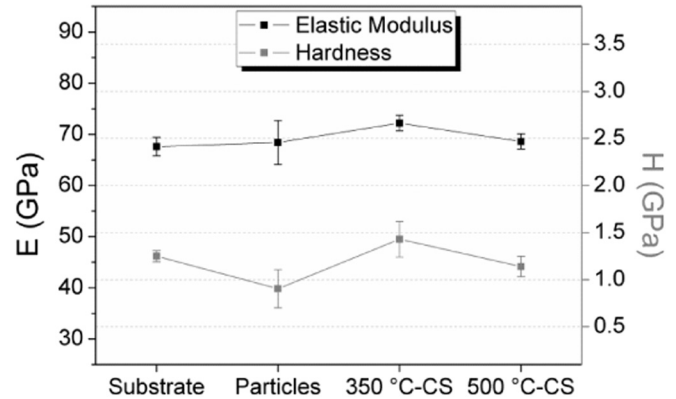


Fig. 12. The elastic modulus (E) and hardness (H) measured by the depth sensing indentation on the Al 2024 T351 substrate, Al 2024 particles and the Al 2024 CS coatings processed at 350 and 500 °C.

Table 3

Elastic modulus (E) and hardness (H) (at nanoscale and microscale) values of the substrate, powder and coatings.

Material/mechanical property	E (GPa)	Nanohardness H (GPa)	Microhardness HV (GPa)
Substrate	$67.6 \pm 1.8$	$1.25 \pm 0.06$	$1.41 \pm 0.05$
Powder	$68.4 \pm 4.3$	$0.91 \pm 0.20$	–
Coating processed at 350 °C	$72.2 \pm 1.5$	$1.43 \pm 0.19$	$1.50 \pm 0.13$
Coating processed at 500 °C	$68.6 \pm 1.5$	$1.14 \pm 0.11$	$1.36 \pm 0.06$

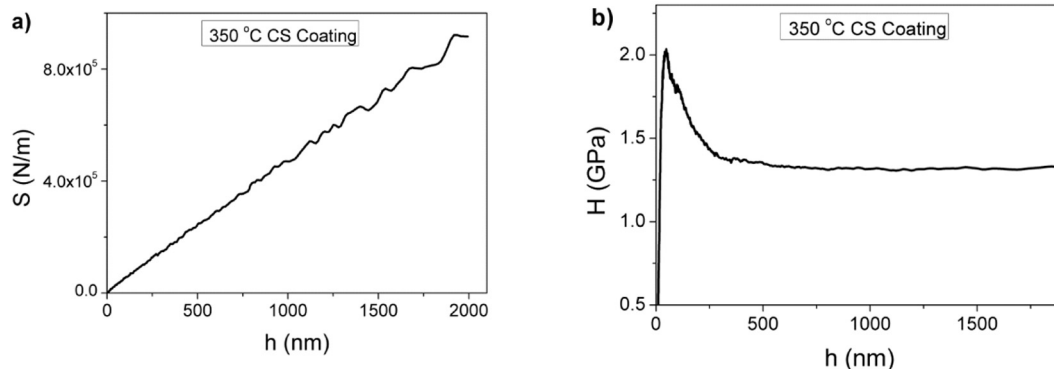


Fig. 11. a) Stiffness (S) vs. penetration depth (h) and b) hardness (H) vs. penetration depth (h) of a representative indentation test conducted on the 350 °C CS Al 2024 coating.



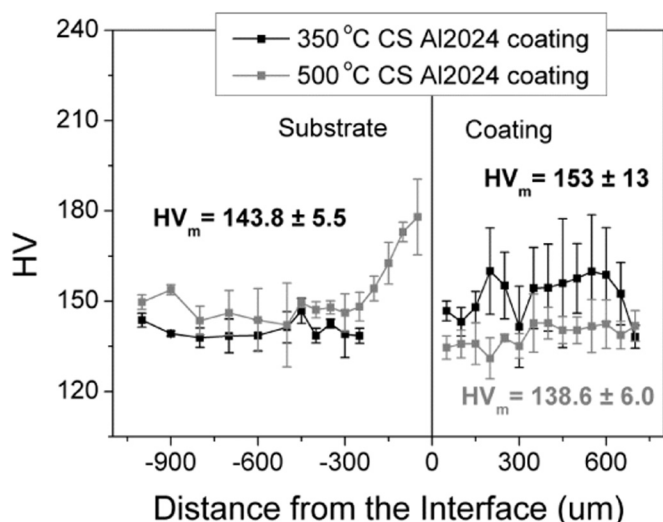


Fig. 13. Vickers microhardness (HV) profile measured on the transversal cross-section of the Al 2024 coatings processed at 350 and 500 °C. The average value of HV ( $HV_m$ ) of the substrate and coatings are indicated.

corresponding to the substrate, both coatings were harder than the bulk Al 2024 T351. From the microstructural perspective, the substrate alloy was clearly different from the coatings. Grains larger than 100 μm with subgrains inside formed the bulk material. No cold worked microstructure was observed in the substrate alloy, which explained the differences in the measured H.

Even though the errors bars were large, the hardness profiles that were carried out in the coatings showed a slight trend (Fig. 13). The hardness was lower in the coatings close to the interface and it was slightly increasing with the distance to the interface. This tendency may be due to the strain gradients that could have occurred during the deposition process as a consequence of the different contribution of the involved basic phenomena in the coatings growth [45].

The results have demonstrated that the deposition temperature has influenced on the degree of work-hardening of the CS coatings, maybe as a consequence of the different particle velocity [38]. However, both CS coatings showed similar microstructural phases independently of the deposition temperature. Conversely, the increase in H with reference to the initial feedstock powder and to the substrate material suggested that both coating deposition conditions were favorable. The obtained mechanical properties were in accordance with the initial hypothesis in which the CS Al 2024 coating properties should be similar to those of the bulk material. Therefore, the present results support the investigation of the Al 2024 CS coatings for aeronautical repairing applications and promote the study of the wear and corrosion behavior of these coatings.

## 6. Conclusions

This work investigates the microstructure and mechanical properties of CS Al 2024 coatings processed at temperatures of 350 and 500 °C. From this study, the following conclusions are drawn:

- Coatings with low porosity and a good contact interface at the substrate and between particles are obtained using the 500 °C and 350 °C deposition temperatures.
- Up to a 500 °C CS process can be performed with satisfactory process reliability and stability. A SOD of 20 mm combined with appropriate travel speed avoids detrimental effects on the base material caused by the enhanced heat input and ensures optimized coating growth conditions.
- Increasing the gas temperature does not induce modifications to the

phase composition.

- The coatings exhibited a work hardened microstructure formed by small subgrains that accommodate the dislocations formed during spraying.
- The coating processed at 500 °C presented a less work hardened microstructure and, consequently, its H was lower than the values obtained for the coating processed under conventional conditions.
- The CS Al 2024 coatings at 500 °C could be adequate for the maintenance and overhaul of Al components used in the aeronautical industry. The corrosion and wear behavior of these coatings should be analyzed to evaluate the possible advantages in the behavior of the repaired components against the most important degradation mechanisms in these materials.

## Acknowledgements

This work was supported by the European Union's Seventh Framework Programme under grant ACS3-GA-2013-605207 (CORSAIR project) and by the Spanish government under grants MAT2013-41784-R (REMACOLDS) and MAT2016-76928-C2-2-R (DURESPRAY).

## References

- [1] J.E. Hatch, *Aluminum: Properties and Physical Metallurgy*, 10th pr. ASM international, Ohio, 2005.
- [2] W. Cassada, J. Liu, J. Staley, *Aluminum alloys for aircraft structures*, Adv. Mater. Process. 160 (2002) 27–29.
- [3] L. Pawłowski, *The Science and Engineering of Thermal Spray Coatings*, 2nd ed., John Wiley & Sons, The Atrium, 1995.
- [4] M. Yandouzi, S. Gaydos, D. Guo, R. Ghelichi, B. Jodoin, *Aircraft skin restoration and evaluation*, J. Therm. Spray Technol. 23 (2014) 1281–1290.
- [5] V.K. Champagne, *The Cold Spray Materials Deposition Process: Fundamentals and Applications*, 1st ed., Woodhead Publishing, 2007.
- [6] A. Papyrin, V. Kosarev, S. Klinkov, A. Alkhimov, V.M. Fomin, *Cold Spray Technology*, 1st ed., Elsevier Ltd, Amsterdam, The Netherlands, 2007.
- [7] V. Champagne, D. Helfrich, *Critical assessment 11: structural repairs by cold spray*, Mater. Sci. Technol. 31 (2015) 627–634.
- [8] J. Villafuerte (Ed.), *Modern Cold Spray: Materials, Process, and Applications*, 1st ed., Springer, 2015.
- [9] S. Yin, Y. Xie, X. Suo, H. Liao, X. Wang, *Interfacial bonding features of Ni coating on Al substrate with different surface pretreatments in cold spray*, Mater. Lett. 138 (2015) 143–147.
- [10] K. Spencer, V. Luzin, N. Matthews, M.X. Zhang, *Residual stresses in cold spray Al coatings: the effect of alloying and of process parameters*, Surf. Coat. Technol. 206 (2012) 4249–4255.
- [11] Y. Tao, T. Xiong, C. Sun, L. Kong, X. Cui, T. Li, G.L. Song, *Microstructure and corrosion performance of a cold sprayed aluminium coating on AZ91D magnesium alloy*, Corros. Sci. 52 (2010) 3191–3197.
- [12] C.W. Ziemian, M.M. Sharma, B.D. Bouffard, T. Nissley, T.J. Eden, *Effect of substrate surface roughening and cold spray coating on the fatigue life of AA2024 specimens*, Mater. Des. 54 (2014) 212–221.
- [13] W.Y. Li, R.R. Jiang, C.J. Huang, Z.H. Zhang, Y. Feng, *Effect of cold sprayed Al coating on mechanical property and corrosion behavior of friction stir welded AA2024-T351 joint*, Mater. Des. 65 (2015) 757–761.
- [14] W.B. Choi, L. Li, V. Luzin, R. Neiser, T. Gnäupel-Herold, H.J. Prask, S. Sampath, A. Gouldstone, *Integrated characterization of cold sprayed aluminum coatings*, Acta Mater. 55 (2007) 857–866.
- [15] R. Ghelichi, D. MacDonald, S. Bagherifard, H. Jahed, M. Guagliano, B. Jodoin, *Microstructure and fatigue behavior of cold spray coated Al5052*, Acta Mater. 60 (2012) 6555–6561.
- [16] M.R. Rokni, C.A. Widener, V.R. Champagne, *Microstructural stability of ultrafine grained cold sprayed 6061 aluminum alloy*, Appl. Surf. Sci. 290 (2014) 482–489.
- [17] M.R. Rokni, C.A. Widener, G.A. Crawford, *Microstructural evolution of 7075 Al gas atomized powder and high-pressure cold sprayed deposition*, Surf. Coat. Technol. 251 (2014) 254–263.
- [18] M.R. Rokni, C.A. Widener, G.A. Crawford, M.K. West, *An investigation into microstructure and mechanical properties of cold sprayed 7075 Al deposition*, Mater. Sci. Eng. A 625 (2015) 19–27.
- [19] M.R. Rokni, C.A. Widener, A.T. Nardi, V.K. Champagne, *Nano crystalline high energy milled 5083 Al powder deposited using cold spray*, Appl. Surf. Sci. 305 (2014) 797–804.
- [20] T. Stoltenhoff, H. Kreye, H.J. Richter, *An analysis of the cold spray process and its coatings*, J. Therm. Spray Technol. 11 (2002) 542–550.
- [21] T. Schmidt, F. Gaertner, H. Kreye, *New developments in cold spray based on higher gas and particle temperatures*, J. Therm. Spray Technol. 15 (2006) 488–494.
- [22] G. Bae, J. Il Jang, C. Lee, *Correlation of particle impact conditions with bonding, nanocrystal formation and mechanical properties in kinetic sprayed nickel*, Acta Mater. 60 (2012) 3524–3535.
- [23] P. Cavaliere, ed, *Cold-Spray Coatings: Recent Trends and Future Perspectives*,

- Springer, 2017.
- [24] G.G. Vander Voort, Specimen preparation for image analysis, in: J.J. Friel (Ed.), *Pract. Guid. to Image Anal*, ASM International, 2000, p. 59.
  - [25] ASTM Standard E1382, Test Methods for Determining Average Grain Size Using Semiautomatic and Automatic Image Analysis, 97 ASTM Int., 2014, pp. 1–24.
  - [26] ASTM Standard E112-12, Standard Test Methods for Determining Average Grain Size, E112-12 ASTM Int., 2012, pp. 1–27.
  - [27] W.C. Oliver, G.M. Pharr, An improved technique for determining hardness and elastic modulus using load and displacement sensing indentation experiments, *J. Mater. Res.* 7 (1992) 1564–1583.
  - [28] W.C. Oliver, G.M. Pharr, Measurement of hardness and elastic modulus by instrumented indentation: advances in understanding and refinements to methodology, *J. Mater. Res.* 19 (2004) 3–20.
  - [29] C. Chang, M.A. Garrido, J. Ruiz-Hervias, J. Rodríguez, On the possibility of reducing the pile-up effect on the Berkovich instrumented indentation tests, *Int. J. Mech. Sci.* 121 (2017) 181–186.
  - [30] A.C. Fischer-Cripps, *Nanoindentation*, 3rd Ed., Springer, New York, USA, 2011.
  - [31] W.D. Nix, H.J. Gao, Indentation size effects in crystalline materials: a law for strain gradient plasticity, *J. Mech. Phys. Solids* 46 (1998) 411–425.
  - [32] H. Li, R.C. Bradt, The microhardness indentation load/size effect in rutile and cassiterite single crystals, *J. Mater. Sci.* 28 (1993) 917–926.
  - [33] Z. Shen, C. Liu, Q. Ding, S. Wang, X. Wei, L. Chen, J. Li, Z. Zhang, The structure determination of  $\text{Al}_{20}\text{Cu}_2\text{Mn}_3$  by near atomic resolution chemical mapping, *J. Alloys Compd.* 601 (2014) 25–30.
  - [34] Z. Huda, N.I. Taib, T. Zaharinie, Characterization of 2024-T3: an aerospace aluminum alloy, *Mater. Chem. Phys.* 113 (2009) 515–517.
  - [35] A. Moridi, S.M. Hassani-Gangaraj, M. Guagliano, M. Dao, Cold spray coating: review of material systems and future perspectives, *Surf. Eng.* 30 (2014) 369–395.
  - [36] L. Ajdelsztajn, A. Zúñiga, B. Jodoin, E.J. Lavernia, Cold gas dynamic spraying of a high temperature Al alloy, *Surf. Coat. Technol.* 201 (2006) 2109–2116.
  - [37] G.E. Totten, D.S. MacKenzie, *Handbook of Aluminum: Volume 2: Alloy Production and Materials Manufacturing*, 1st ed., CRC Press, New York, 2003.
  - [38] T. Schmidt, H. Assadi, F. Gärtner, H. Richter, T. Stoltenhoff, H. Kreye, T. Klassen, From particle acceleration to impact and bonding in cold spraying, *J. Therm. Spray Technol.* 18 (2009) 794–808.
  - [39] A. Sova, A. Okunkova, S. Grigoriev, I. Smurov, Velocity of the particles accelerated by a cold spray micronozzle: experimental measurements and numerical simulation, *J. Therm. Spray Technol.* 22 (2013) 75–80.
  - [40] P.H. Suegama, C.S. Fugivara, A.V. Benedetti, J. Fernández, N. Espallargas, J. Delgado, J.M. Guilemany, New research on electrochemistry, *Nov. Sci. Publ.* (2007) 113–151.
  - [41] G. Huang, H. Wang, X. Li, L. Xing, J. Zhou, Deposition efficiency of low pressure cold sprayed aluminum coating, *Mater. Manuf. Process.* (2017) 1–7.
  - [42] N.J.E. Adkins, P. Tsakirooulos, Design of powder metallurgy aluminium alloys for applications at elevated temperatures part 1 microstructure of high pressure gas atomized powders, *Mater. Sci. Technol.* 7 (1991) 334–340.
  - [43] G.E. Dieter, *Mechanical Metallurgy*, SI Metric, McGraw-Hill Book Company, London, 1988.
  - [44] Q. Wang, N. Birbilis, M.X. Zhang, Interfacial structure between particles in an aluminum deposit produced by cold spray, *Mater. Lett.* 65 (2011) 1576–1578.
  - [45] T.H.V. Steenkiste, J.R. Smith, R.E. Teets, Aluminum coatings via kinetic spray with relatively large powder particles, *Surf. Coat. Technol.* 154 (2002) 237–252.